RSC Advances

PAPER

View Article Online
View Journal | View Issue

Cite this: *RSC Adv.*, 2025, **15**, 22411

Green fabrication of graphene aerogel using pineapple juice for efficient degradation of synthetic dyes†

Lu Thi Mong Thy,[a] Nguyen Le Hoai Thanh,[b] Nguyen Van Quy,[b] Do Thuy Khanh Linh,[b] Tran Thi Nhung,[b] Anh-Tam Nguyen,[c] Dai-Viet N. Vo,[c] Le Kim Hoang Pham [c] and Ly Tan Nhiem *[b]

Synthetic dyes pose significant environmental and health concerns due to their complex chemical structures and resistance to degradation. Conventional water treatment systems often incorporate chemical tanks and aerobic treatment to achieve complete dye removal, however, these methods typically result in high construction costs and operational complexity. In this study, graphene aerogel (GA) incorporated with Fe_3O_4 nanoparticles (NPs) was fabricated using pineapple juice as a reducing agent, denoted as GA@Fe_3O_4. Vibrating sample magnetometry results showed that the saturation magnetization values of Fe_3O_4 and GA@Fe_3O_4 were 58.59 and 18.02 emu g^{-1}, respectively, indicating that the as-prepared GA@Fe_3O_4 could be effectively recovered using an electromagnetic field. Further investigation using scanning electron microscopy and transmission electron microscopy revealed that the Fe_3O_4 NPs, sized approximately 17–20 nm, were evenly distributed on the GA surface. Notably, the GA@Fe_3O_4, with macropore structures ranging from 2 to 10 μm, exhibited degradation capabilities for reactive dye RB222. Kinetic models were subsequently established, demonstrating that the degradation followed a zero-order kinetic model with $R^2 = 0.9863$, and a rate constant $k = 0.07984$ (mg L^{-1} min^{-1}). The GA@Fe_3O_4 synthesized in this study demonstrated high potential as an effective adsorbent for the degradation of synthetic dyes in the textile industry. Furthermore, pineapple juice, used as a green reducing agent, was demonstrated to be a viable alternative to other harmful reductants commonly used in the preparation of GA.

Received 24th April 2025
Accepted 22nd June 2025

DOI: 10.1039/d5ra02875b

rsc.li/rsc-advances

Introduction

The textile industry is a significant contributor to synthetic dye pollution, which has negatively impacted human life and the environment.[1,2] These dyes in industrial wastewater are difficult to degrade due to their resistance to light, heat, and other oxidizing agents, leading to severe water pollution.[3,4] Conventionally, synthetic dyes can be treated using electrocoagulation,[5] anaerobic biological methods,[6] and advanced oxidation,[7] in comprehensive wastewater treatment systems. However, such advanced systems are often complex to construct and involve high operational costs. Alternatively, a wide range of adsorbent materials have been developed for the effective adsorption and/or degradation of synthetic dyes.[8,9] Among them, graphene aerogel (GA) materials, fabricated from chemically derived graphene oxide (GO), show promise in wastewater treatment due to their superior properties,[10,11] such as high adsorption capacity, excellent chemical and thermal stability, and ease of recovery. Several approaches have been employed to fabricate GA, including hydrothermal reduction,[12] chemical reduction,[13] and template-directed reduction.[14] Typically, the starting GO undergoes a reduction process, losing its functional groups, followed by gelation, where the reduced GO flakes are assembled together through cross-linking agents and/or reducing agents to form 3D hydrogel structures.[14] These methods require high energy input and the use of strong reductants to achieve the desired 3D structures, which hinders the practical applicability of such approaches in addressing dye pollution. To enhance environmental friendliness, plant extracts have been explored as green reducing agents for GA fabrication. Various extracts, such as *Plectranthus amboinicus*,[15] and grape seed extract,[16] have been utilized in this regard. A promising candidate for this purpose is pineapple juice, which contains bioactive compounds such as alkaloids, tannins, saponins, flavonoids, vitamin C, and polyphenols. Among these, vitamin

[a]*Ho Chi Minh City University of Industry and Trade, 140 Le Trong Tan Street, Tay Thanh Ward, Tan Phu District, Ho Chi Minh City, Vietnam*

[b]*Faculty of Chemical and Food Technology, Ho Chi Minh City University of Technology and Education, 01 Vo Van Ngan Street, Linh Chieu Ward, Thu Duc City, Ho Chi Minh City, Vietnam*

[c]*Institute of Applied Technology and Sustainable Development, Nguyen Tat Thanh University, Ho Chi Minh City 755414, Vietnam*

† Electronic supplementary information (ESI) available. See DOI: https://doi.org/10.1039/d5ra02875b

C,[17] and polyphenols,[18] have been widely used as reducing agents in the synthesis of nanoparticles. Therefore, pineapple juice is expected to exhibit favorable characteristics as a reducing agent in the fabrication of GA, while also acting as an effective cross-linker for stabilizing the resulting graphene aerogel network. In addition, Fe_3O_4 nanoparticles (NPs), known for their peroxidase-mimic catalytic reactivity, have been commonly used to generate free hydroxyl radicals ($^{\bullet}OH$) in Fenton-like reactions.[19] These radicals are highly effective in decomposing organic molecules such as synthetic dyes.[20] Fe_3O_4 NPs also exhibit superparamagnetic properties,[19] with a saturation magnetization of approximately 20–50 emu g^{-1} for particles in the size range of 5–10 nm, enabling strong interactions with external magnetic fields. Proper integration of Fe_3O_4 NPs into the GA network is expected to overcome the natural aggregation tendency of the nanoparticles, enhancing their catalytic properties.[21,22] Furthermore, GA incorporated with Fe_3O_4 NPs offers ease of recovery and handling, particularly in aquatic environments. In this study, pineapple juice was used as a reducing agent for the preparation of GA with the assistance of polyvinylpyrrolidone (PVP). Fe_3O_4 NPs were also embedded within the GA network, enabling the recovery of GA using a magnetic field, and the resulting GA was successfully employed for degradation of reactive dyes.

Experimental

Materials

Graphite (99.5%), sodium nitrite ($NaNO_2$, 99%), acid sulfuric (H_2SO_4, 98%), potassium permanganate ($KMnO_4$, 99.5%), ammonium hydroxide (NH_4OH, 25%), ferrous chloride ($FeCl_2$, 98%), ferric chloride ($FeCl_3$, 98%), and polyvinylpyrrolidone (PVP, 95%) were acquired from Sigma-Aldrich. Reactive Blue 222 (RB222) was obtained from Alfa Chemistry. Ethanol (C_2H_5OH, 99.5%), and acetone (99.7%) were purchased from Chemsol (Vietnam). Hydrogen peroxide (H_2O_2, 30%) was obtained from Merck (Germany). De-ionized (DI) water was used in all experiments.

Preparation of pineapple juice

First, pineapple raw materials were harvested and pre-treated before being pressed to obtain a juice mixture. The juice was then centrifuged at 5000 rpm for 20 minutes to obtain clear pineapple juice, which was ready for use. The juice sample was subsequently analyzed for total polyphenols (Tables S1, S2 and Fig. S1†), and vitamin C content (Table S3†), following the methods described in the ESI.† The measured concentrations were 44.98 ± 0.85 mg per 100 mL for vitamin C and 579.83 ± 0.86 μg GAE per mL juice for total polyphenols.

Preparation of graphene aerogel

Graphene oxide (GO) was synthesized using the modified Hummers' method,[23,24] employing $NaNO_2$ and $KMnO_4$ as oxidizing agents, and using graphite (Gi) as a starting material. Meanwhile, Fe_3O_4 nanoparticles (NPs) functionalized with citric acid (denoted as Fe_3O_4@COOH) were prepared *via* the co-precipitation method,[19] as described in detail in the ESI.†

For the preparation of graphene aerogel, a 20 mL GO dispersion (10 mg mL^{-1}) was subjected to ultrasonication for 15 minutes. Subsequently, 100 mg of Fe_3O_4@COOH was dispersed into the GO suspension to achieve a final concentration of 5 mg mL^{-1}. The mixture was then heated to 90 °C using an ethylene glycol heating bath, followed by the addition of 20 mg of PVP to obtain a final concentration of 1 mg mL^{-1}. The solution was stirred for several minutes to ensure complete dissolution of PVP. Next, 5 mL of the resulting homogeneous mixture was transferred into a plastic tube, and 1 mL of DI water along with 4 mL of ethanol was added. The solution was thoroughly shaken and sonicated for 10 minutes to enhance dispersion. Subsequently, 3 mL of pineapple juice was introduced into each tube containing the GO suspension, and the mixture was shaken for 1 minute to promote uniform distribution. The tubes were then incubated at 90 °C for 4 hours to facilitate gel formation. After completion of the heating process, the tubes were removed, and the formation of a gel-like structure, identified as graphene hydrogel, was observed. The hydrogel samples were thoroughly immersed in DI water and washed multiple times to eliminate residual ethanol. After purification, 10 mL of DI water was added to each sample, and they were frozen at −40 °C overnight. Finally, the solidified hydrogel samples were subjected to freeze-drying to remove water, yielding an ultra-light and highly porous material, referred to as graphene aerogel decorated with Fe_3O_4 NPs (GA@Fe_3O_4). Pristine graphene aerogel (denoted as GA) was also fabricated following the same procedure described above, but without the addition of Fe_3O_4 NPs.

Characterization

Fourier-transform infrared spectroscopy (FTIR, PerkinElmer) was employed to identify the functional groups present in the synthesized materials. X-ray diffraction (XRD, D8 Phaser, Bruker) was used to analyze the crystallographic structure of GO and the aerogel materials, utilizing a Cu-Kα radiation source with a wavelength of 0.154 nm. X-ray photoelectron spectroscopy (XPS, PHI 5000 VersaProbe II) with an energy source of 187 eV was used to investigate the chemical composition and bonding states of GA@Fe_3O_4. The morphological characteristics of the as-prepared materials were examined using field-emission scanning electron microscopy (FE-SEM, Hitachi S-4800) and transmission electron microscopy (TEM, JEM-1010, JEOL). Raman spectroscopy (RA-TN05, 532 nm, Horiba Scientific) was conducted to analyze the structural vibrations within the materials. The Brunauer–Emmett–Teller (BET) was used to determine the pores size by analyzing N_2 adsorption–desorption isotherm. The magnetic properties of Fe_3O_4 nanoparticles were assessed using a vibrating sample magnetometer (VSM, MicroSense). Additionally, the UV-vis absorbance spectra were recorded using a UV-vis spectrometer (UH5300, Hitachi).

Investigation of the dye degradation efficiency of GA@Fe_3O_4

First, a 40 mL solution of reactive dye RB222 was prepared in DI water at an initial concentration (C_0) of 43.44 mg L^{-1} in an

Erlenmeyer flask. This concentration of RB222 is considered moderate in textile wastewater. RB222 was selected as the model dye in this study because it is widely recognized as one of the most commonly used reactive dyes in the textile industry.[25,26] It contains both vinyl sulfone and chlorotriazine functional groups,[26] making it a suitable representative for investigating dye degradation and removal processes. A cubic piece of GA@Fe_3O_4 (200 mg) was then immersed in the dye solution. The mixture was placed in a horizontal shaker set at 150 rpm, and 100 μL of 30% H_2O_2 was added to initiate the degradation process. The shaking was continued throughout the experiment. At specific time intervals of 30, 60, 90, 120, 150, 180, 210, 240, and 270 minutes, 4 mL aliquots of the solution were withdrawn from the flask for analysis. The UV-vis absorbance of the solution was measured at 612 nm to determine the residual concentration of RB222 (C_t) at each time point. Each data point represents the average of five independent experiments conducted using as-prepared materials from five different batches. This method is commonly used in other studies to quantify residual dye concentrations.

Results and discussion

The chemical structures of the as-prepared materials were analyzed using FTIR spectroscopy, as shown in Fig. 1a. The FTIR spectrum of Gi exhibits absorption signals due to differences in charge states between carbon atoms, leading to minimal electric dipole induction. Three characteristic peaks observed at 1975, 2025, and 2158 cm^{-1} correspond to the vibrational modes of C=C, C≡C, and N≡C bonds, respectively, within the Gi network.[27] The presence of C≡C and N≡C bonds is attributed to impurities introduced during the production process of Gi. Meanwhile, the FTIR spectrum of GO displayed characteristic peaks at 684, 1030, 1225, 1409, 1616, 1727, and 3200 cm^{-1}, corresponding to the bending vibration of C–H, stretching vibration of C–O (alkoxy), stretching vibration of C–O–C (epoxy), bending vibration of C–O–H, stretching vibration of C=C in the aromatic ring, stretching vibration of C=O, and the O–H stretching vibration in hydroxyl (–OH) groups, respectively.[28–30] These results confirm the successful oxidation and functionalization of Gi *via* the Hummers' method. For GA, the spectrum still exhibited peaks corresponding to oxygen-containing functional groups. However, the intensities of these peaks were significantly lower than those observed in GO, indicating the occurrence of a reduction process during gelation. In the spectrum of GA@Fe_3O_4, the characteristic peaks of GA remained present. Notably, a dominant peak at 546 cm^{-1} was assigned to the Fe–O vibration in Fe_3O_4.[31] Additionally, peaks at 1409 and 1590 cm^{-1}, corresponding to the bending vibration of C–O–H and the stretching vibration of C=O in carboxyl (–COOH) groups, respectively, confirmed the successful incorporation of Fe_3O_4@COOH into the as-prepared GA@Fe_3O_4.[30,31] As demonstrated, GO contains abundant oxygenated groups that increase hydrophilicity and adsorption of polar dyes. Meanwhile, reduced GO restores the sp^2 carbon network, enhancing charge separation in catalyst (*e.g.*, GA@Fe_3O_4) and promoting

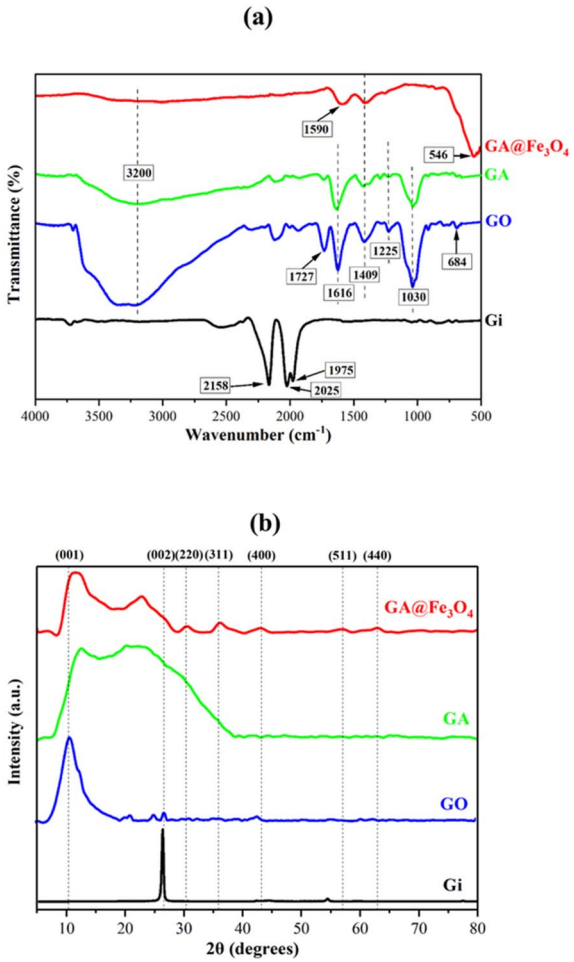

Fig. 1 Chemical structures of the as-prepared materials, (a) FTIR spectra, and (b) XRD spectra.

efficient generation of reactive species ($^{\bullet}OH$, O_2^{-}) for dye degradation.[32,33]

To evaluate the reduction efficiency of oxygen-containing groups during the transformation from GO to GA, the areas under the band ranging from 927 to 1486 cm^{-1} were calculated, as illustrated in Fig. S6.† The corresponding RE was determined using the following relationship:[32,34]

$$\mathrm{RE}\ (\%) = \frac{A_{\mathrm{GO}} - A_{\mathrm{GA}}}{A_{\mathrm{GO}}} \times 100,$$

where A_{GO} and A_{GA} represent the areas under the specified wavenumber band for GO and GA, respectively. The RE was calculated to be 45.3%, which is considered favorable for dye degradation applications. This is because the GA must retain sufficient hydrophilicity to effectively capture dye molecules from aqueous solutions. On the other hand, the partial reduction of oxygen-containing groups renders the material more hydrophobic, inducing the formation of a three-dimensional porous network with a more rigid arrangement of macroporous channels. This structural transformation plays a crucial role in facilitating molecular diffusion and enhancing the adsorption of dye molecules. Therefore, the degree of GO

reduction achieved in this study is expected to exhibit superior performance in dye degradation.

The crystalline structures and inter-layer spacing of the as-prepared materials were analyzed using XRD patterns (Fig. 1b). The XRD spectrum of Gi exhibited a peak at $2\theta \approx 26.94°$, corresponding to the (002) crystal lattice, which is characteristic of Gi material.[35,36] Meanwhile, the spectrum of GO, an oxidized form of Gi, displayed a peak at $2\theta \approx 10.90°$, corresponding to the (001) lattice plane.[37] This strongly indicates that the interlayer distance within the Gi structure expanded upon the introduction of oxygen-containing functional groups during oxidation. For GA, two diffraction peaks appeared at $2\theta \approx 10.54°$ and 23.59°, suggesting that some oxygen-containing functional groups in GO were reduced during the gelation process, subsequently causing the graphene layers to move closer together. These XRD patterns are consistent with previous studies.[38,39] In the spectrum of GA@Fe_3O_4, five additional characteristic peaks of Fe_3O_4 appeared at $2\theta \approx 30.44°$, 35.91°, 43.19°, 57.11°, and 62.99°, corresponding to the (220), (311), (400), (511), and (440) crystal planes, respectively.[19,40] In addition to TEM and Raman results discussed in the ESI (Fig. S2 and S3),† the incorporation of Fe_3O_4@COOH with GO proved to be crucial for the fabrication of GA@Fe_3O_4. The redundant carboxyl groups acted as anchoring sites for the firm attachment of Fe_3O_4@COOH onto GO *via* hydrogen bonding and molecular interactions.[41,42] Importantly, the I_D/I_G ratio for GO is 0.96, whereas for GO@Fe_3O_4, it increases to 1.18. This enhancement indicates that the incorporation of Fe_3O_4 NPs induces greater structural disorder within the graphene oxide matrix.[43,44] These interactions remained stable during the reduction process facilitated by pineapple juice, leading to strong signals of Fe_3O_4 NPs observed in both the FTIR and XRD spectra discussed above. The chemical structures of GA@Fe_3O_4 were further confirmed using XPS. The spectra of binding energies (BE) related to valence orbitals in GA@Fe_3O_4 are shown in Fig. 2, and deconvolution was conducted to clarify the chemical states. Four different core-level orbitals were examined, including C 1s, O 1s, N 1s, and Fe 2p. In the C 1s spectrum, the dominant peak was deconvoluted into three smaller components at BE = 283.29, 284.88, and 287.08 eV, corresponding to C–C/C=C, C–N, and C–O/C=O bonds, respectively.[45–47] The presence of C–N bonds can be attributed to nitrogen-containing impurities in the original graphite, as previously discussed in the FTIR results. Similarly, the O 1s spectrum was deconvoluted into three peaks at BE = 530.40, 531.50, and 532.30 eV, corresponding to C=O, C–O, and O–H bonding states, respectively.[48] Interestingly, the N 1s spectrum revealed three distinct peaks at BE = 398.48, 399.95, and 400.65 eV, assigned to N–C, N–O, and N–H bonds, respectively.[49] The relatively low intensity of these peaks compared to those in the C 1s and O 1s spectra suggests that only a small fraction of nitrogen-containing species, likely from residual amino acids present in the pineapple juice, remains in the final product. The XPS spectrum of Fe 2p orbitals was deconvoluted into smaller peaks corresponding to the Fe^{2+} and Fe^{3+} oxidation states present in Fe_3O_4. The Fe^{2+} $2p_{3/2}$ peak appeared at 709.5 eV, while the Fe^{3+} $2p_{3/2}$ peak was observed at 711.5 eV.[50] Similarly, the Fe^{2+} $2p_{1/2}$ and Fe^{3+} $2p_{1/2}$ peaks were located at 723.5 eV and 724.7 eV, respectively.[51] Additionally, satellite peaks associated with the mixed Fe^{2+}/Fe^{3+} oxidation states were identified at BE of 718.4 eV and 732.3 eV.[50,51] These results confirm the presence of Fe_3O_4 with a mixed-valence state. As the results, the chemical bonding states demonstrated by FTIR were confirmed by XPS, validating the successful fabrication of GA@Fe_3O_4. For comparison, the XPS spectra of GA without Fe_3O_4 are also provided in the ESI.†

The morphology of GA@Fe_3O_4 was examined using SEM, as shown in Fig. 3. The aerogels exhibit a highly interconnected 3D porous framework, formed through the self-assembly of reduced graphene oxide (RGO) sheets. The pore walls consist of overlapping RGO layers, creating a foam-like structure. The presence of macropores is clearly observed, exhibiting a wide range of sizes and shapes, typically spanning from 2 to 10 μm. The Fe_3O_4 NPs are non-uniformly distributed within the porous structure of the GA. In some regions, agglomeration occurs, leading to areas with higher concentrations of Fe_3O_4 clusters. Additionally, the edges and wrinkles of the graphene sheets tend to exhibit a greater accumulation of nanoparticles, which may be attributed to stronger electrostatic interactions or van der Waals forces.[52,53]

Further investigation using BET was conducted, as shown in Fig. 4. The adsorption–desorption isotherm exhibits a hysteresis loop, which is a characteristic feature of capillary condensation in mesoporous materials[54,55] (Fig. 4a). The results confirm that GA@Fe_3O_4 follows a type IV isotherm, indicating the presence of mesopores with cylindrical pore structures. According to the Barrett–Joyner–Halenda (BJH) pore size distribution analysis (Fig. 4b), the peak in the differential pore volume curve (red) around 20–50 Å further supports the mesoporous nature of the material. Additionally, some larger pores (~100 Å and beyond) are present, though they contribute minimally to the overall pore volume. To investigate the micropores present in GA@Fe_3O_4, the Dubinin–Astakhov (DA) method was applied (Fig. 4c). The results indicated that the pore sizes were primarily distributed around a peak at 25 Å, suggesting that the aerogel material does not contain a high proportion of micropores (<20 Å). As a result, the as-prepared GA@Fe_3O_4 exhibits a hierarchical porous structure, comprising both macropores and mesopores. The coexistence of these pores enhances mass transport, surface area, and accessibility.

The magnetic properties of GA@Fe_3O_4 were investigated using VSM. As shown in Fig. 5, the magnetization curves of both Fe_3O_4 NPs and GA@Fe_3O_4 exhibit a similar shape, symmetrical about the origin, indicating typical superparamagnetic behavior.[22] The saturation magnetization of Fe_3O_4 NPs was measured to be 58.59 emu g^{-1}, while the GA@Fe_3O_4 exhibited a lower value of 18.02 emu g^{-1}. This reduction in saturation magnetization is attributed to the non-magnetic graphene aerogel matrix, which dilutes the magnetic phase. Nevertheless, despite the significant decrease, the obtained value still provides sufficient magnetic responsiveness, enabling the efficient and rapid recovery of GA@Fe_3O_4 under an external magnetic field. These results are consistent with previously

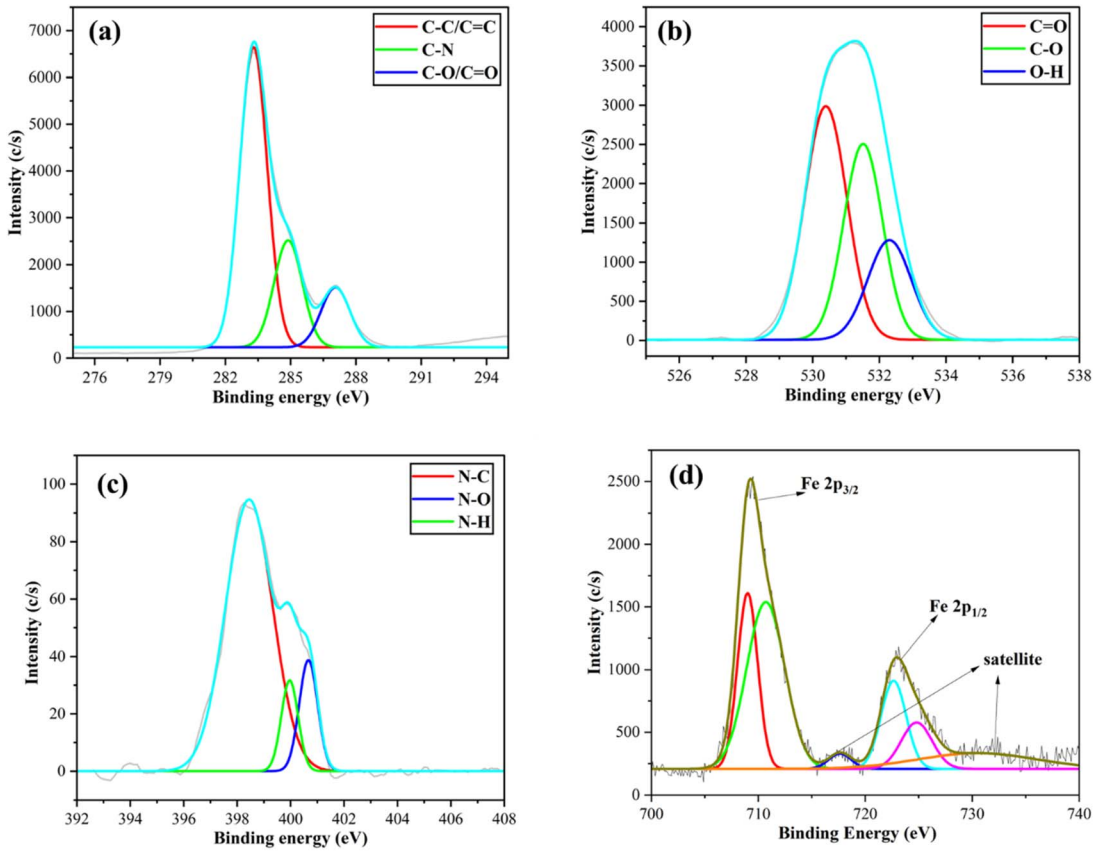

Fig. 2 XPS spectra of GA@Fe_3O_4 with orbitals (a) C 1s, (b) O 1s, (c) N 1s, and (d) Fe 2p.

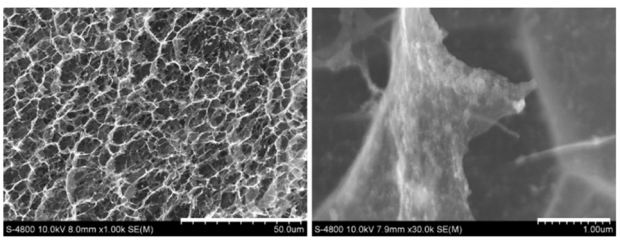

Fig. 3 SEM images of the GA@Fe_3O_4 at two different scale bars, 50 μm (left) and 1 μm (right).

reported values in the literature,[56,57] further confirming the successful incorporation of Fe_3O_4 into the aerogel matrix. Vitamin C and polyphenols found in pineapple juice are known for their reducing properties as mentioned earlier. Vitamin C, as a reducing agent, is a well-established approach in nanomaterial synthesis, particularly in metal ion reduction.[58,59] Meanwhile, polyphenols, a broad class of naturally occurring compounds rich in hydroxyl groups, also serve as effective reducing agents in various applications.[60,61] Their electron-donating capacity, attributed to the presence of phenolic hydroxyl groups, makes them powerful antioxidants and reducing agents. The presence of these two naturally occurring reducing agents in pineapple juice facilitates the reduction of GO, leading to the formation of GA@Fe_3O_4. Notably, the reduction process was demonstrated to preserve the intrinsic properties of Fe_3O_4 NPs, particularly their superparamagnetic behavior.

The as-prepared GA@Fe_3O_4 was employed for the adsorption and degradation of RB222. In this approach, hydroxyl radicals $^{\bullet}OH$ generated on the catalytic surface of Fe_3O_4 NPs facilitate Fenton-like reactions. The redox cycling between Fe^{2+} and Fe^{3+} in Fe_3O_4 enables continuous $^{\bullet}OH$ generation in the presence of hydrogen peroxide (H_2O_2), following the reactions:[19]

$$Fe^{2+} + H_2O_2 \rightarrow Fe^{3+} + {}^{\bullet}OH + OH^- \; k_1 = 40\text{–}80\ M^{-1}\ s^{-1} \quad (1)$$

$$Fe^{3+} + H_2O_2 \rightarrow Fe^{2+} + HO_2^{\bullet} + H^+ \; k_2 = 0.001 - 0.01\ M^{-1}\ s^{-1} \quad (2)$$

$$Fe^{3+} + HO_2^{\bullet} \rightarrow Fe^{2+} + O_2 + H^+ \; k_3 = 3.3 \times 10^7\ M^{-1}\ s^{-1} \quad (3)$$

The abundant Fe^{2+}/Fe^{3+} in Fe_3O_4 enables continuous and efficient $^{\bullet}OH$ generation, which is crucial for oxidative degradation. Hydroxyl radicals $^{\bullet}OH$ are highly reactive and non-selective, attacking a wide range of organic pollutants, breaking them into smaller, less toxic compounds, or ultimately mineralizing them into CO_2 and H_2O.[62,63] RB222, an anthraquinone-based dye widely used in the textile industry, exhibits significant resistance to biodegradation but is susceptible to oxidative degradation by $^{\bullet}OH$ radicals. The degradation

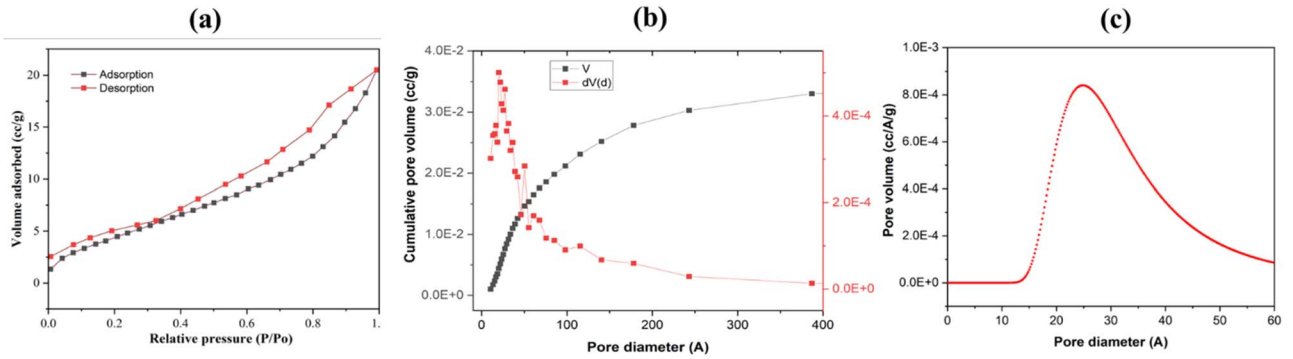

Fig. 4 (a) N_2 adsorption–desorption isotherm of GA@Fe_3O_4, (b) pore size distribution of GA@Fe_3O_4 determined by the BJH adsorption method, (c) pore size distribution of GA@Fe_3O_4 determined by the DA method.

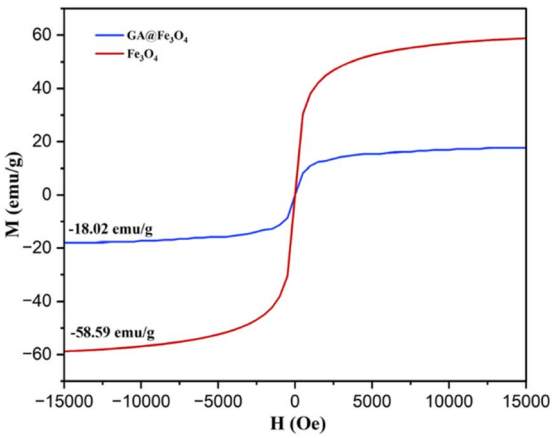

Fig. 5 VSM results for the as-prepared Fe_3O_4@COOH & GA@Fe_3O_4.

of RB222 by ˙OH radicals follows multiple pathways.[64,65] Initially, the radicals attack the electron-rich anthraquinone core, disrupting conjugated π-electron systems and breaking chromophores, leading to decolorization. Subsequently, oxidative cleavage of N=N bonds and sulfonate groups results in the formation of smaller organic intermediates. Continued oxidation promotes further breakdown, leading to complete mineralization, where the dye is fully converted into CO_2, H_2O, and inorganic ions. To evaluate the degradation kinetics, several kinetic models were established as the following:[66,67]

$$\text{Zero-order model, } C_t = C_0 - k_0 t \quad (4)$$

$$\text{First-order model, } \ln(C_t/C_0) = -k_1 t \quad (5)$$

$$\text{Second-order model, } (1/C_t) = (1/C_0) + k_2 t \quad (6)$$

where C_0 and C_t are the reactive dye concentrations (mg L^{-1}) at initial and at reaction time t, respectively, and k_0, k_1, and k_2 are the corresponding rate constants. As shown in Fig. 6, the degradation of RB222 was found to best fit the zero-order kinetic model, with the equation $y = 25.57477 - 0.07984x$, $R^2 = 0.9863$, and a rate constant $k = 0.07984$ (mg L^{-1} min^{-1}), the haft-life time was calculated to be $t_{1/2} = 160.2$ minutes. The zero-order kinetic behavior can be attributed to the excessive concentration of hydroxyl radicals relative to the dye molecules,[68,69] resulting in a constant degradation rate independent of RB222 concentration. This suggests that nanoscale Fe_3O_4 provides a high surface area, facilitating catalytic activity and radical production. Furthermore, as the reaction progresses and RB222 concentration decreases significantly, a transition from first-order to zero-order kinetics is observed, supported by the

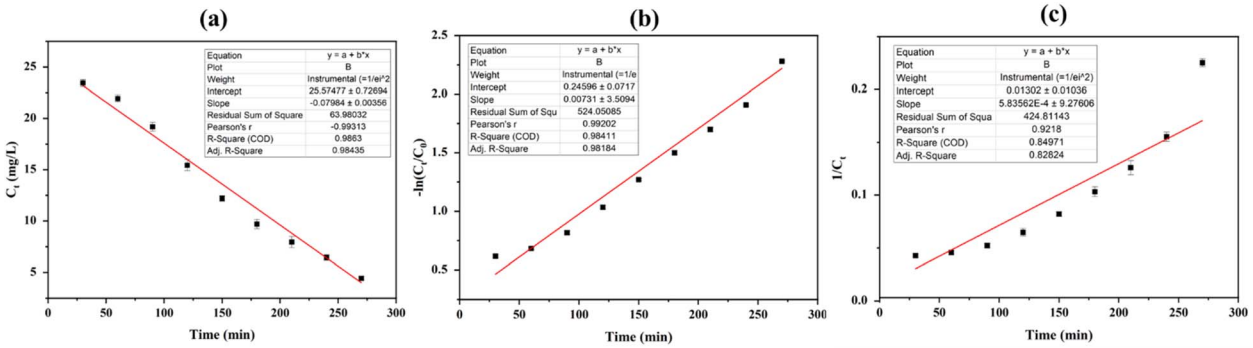

Fig. 6 Plots for RB222 degradation kinetics using GA@Fe_3O_4, (a) zero-order kinetic model, (b) first-order kinetic model, and (c) second-order kinetic model.

fact that the first-order kinetic model also exhibits good linearity, with $R^2 = 0.9841$ and a rate constant of 0.00731 (min^{-1}). In addition to its catalytic efficiency, the Fe_3O_4-based system offers practical advantages, including easy magnetic recovery, which enhances reusability and minimizes secondary pollution. These findings demonstrate GA@Fe_3O_4 provide a promising and effective strategy for wastewater treatment containing dye pollutants. This approach is particularly beneficial in real wastewater treatment applications, where maintaining high degradation rates across various pollutant concentrations is crucial, as wastewater sources are often unpredictable.

Conclusions

In this study, Fe_3O_4 NPs were incorporated into GO through a reduction process using pineapple juice as a reducing agent, resulting in GA@Fe_3O_4. The juice sample was subsequently analyzed for total polyphenol and vitamin C content, which were determined to be 579.83 ± 0.86 μg GAE per mL and 44.98 ± 0.85 mg per 100 mL, respectively. The chemical structures of GA@Fe_3O_4 were characterized using FTIR, XRD, and XPS, revealing the presence of high functionalities in the structures. SEM and BET results indicated that GA@Fe_3O_4 consists of macropores (2–10 μm) and mesopores (20–50 Å), while superparamagnetic behavior was confirmed with a saturation magnetization value of 18.02 emu g^{-1}. Importantly, GA@Fe_3O_4 was demonstrated to be effective in the degradation of reactive dye RB222, following a zero-order kinetic model with R^2 = 0.9863 and a rate constant of $k = 0.07984$ mg L^{-1} min^{-1}, indicating that an excessive amount of hydroxyl radicals relative to the dye molecules was generated. GA@Fe_3O_4 exhibits potential as an efficient material for the degradation of reactive dyes in the textile industry.

Data availability

The data supporting this article have been included as part of the ESI.†

Author contributions

Lu Thi Mong Thy: conceptualization, methodology, initial draft preparation; Nguyen Le Hoai Thanh: investigation, data curation, formal analysis. Nguyen Van Quy: sample preparation; Do Thuy Khanh Linh: analytical measurements; Tran Thi Nhung: figure preparation; Anh-Tam Nguyen: resources; Dai-Viet N. Vo: resources; Le Kim Hoang Pham: instrumentation support; Ly Tan Nhiem: conceptualization, supervision, writing – review & editing, funding acquisition, project administration.

Conflicts of interest

There are no conflicts to declare.

References

1 H. Herbst, *Fordham Int. Law J.*, 2021, **45**, 907.
2 K. Gomes, S. Caucci, J. Morris, E. Guenther and J. Miggelbrink, *Bus. Strategy Dev.*, 2024, **7**, e324.
3 A. E. Oluwalana and N. Chaukura, in *Nano-engineered Materials for Textile Waste Remediation*, ed. A. K. Mishra, Springer Nature, Singapore, 2023, pp. 35–60.
4 E. Altintig, T. Ö. Özcelik, Z. Aydemir, D. Bozdag, E. Kilic and A. Yılmaz Yalçıner, *Int. J. Phytorem.*, 2023, **25**, 1714–1732.
5 Y. Mao, Y. Zhao and S. Cotterill, *Water*, 2023, **15**, 1455.
6 S. Ledakowicz and K. Paździor, *Molecules*, 2021, **26**, 870.
7 C. Gallego-Ramírez, E. Chica and A. Rubio-Clemente, *Water*, 2022, **14**, 2531.
8 A. Haleem, A. Shafiq, S.-Q. Chen and M. Nazar, *Molecules*, 2023, **28**, 1081.
9 E. Murugan, J. N. Jebaranjitham, K. J. Raman, A. Mandal, D. Geethalakshmi, M. D. Kumar and A. Saravanakumar, *New J. Chem.*, 2017, **41**, 10860–10871.
10 K. He, G. Chen, G. Zeng, A. Chen, Z. Huang, J. Shi, T. Huang, M. Peng and L. Hu, *Appl. Catal., B*, 2018, **228**, 19–28.
11 Y. B. Pottathara, H. R. Tiyyagura, Z. Ahmad and K. K. Sadasivuni, *J. Energy Storage*, 2020, **30**, 101549.
12 M. F. Hasan and L. Zhang, *Fibers Polym.*, 2023, **24**, 1553–1572.
13 A. S. Falchevskaya, A. Y. Prilepskii, S. A. Tsvetikova, E. I. Koshel and V. V. Vinogradov, *Chem. Mater.*, 2021, **33**, 1571–1580.
14 G. Nassar, E. Daou, R. Najjar, M. Bassil and R. Habchi, *Carbon Trends*, 2021, **4**, 100065.
15 T. Zheleznichenko, T. Veklich and V. Kostikova, *Rend. Fis. Accad. Lincei*, 2024, **35**, 961–970.
16 J. Borges-Vilches, J. Poblete, F. Gajardo, C. Aguayo and K. Fernández, *J. Mater. Sci.*, 2021, **56**, 16082–16096.
17 R. M. Hassan, *J. Mol. Struct.*, 2022, **1250**, 131575.
18 N. Swilam and K. A. Nematallah, *Sci. Rep.*, 2020, **10**, 14851.
19 L. T. Nhiem, C. H. Q. Quy, H. N. A. Tuan, M. H. Do, J.-S. Noh and Q. T. H. Ta, *Microchem. J.*, 2025, **208**, 112347.
20 A. Mandal, E. Dhineshkumar and T. P. Sastry, *Clean Technol. Environ. Policy*, 2023, **25**, 3285–3302.
21 A. Mandal, E. Dhineshkumar and E. Murugan, *ACS Omega*, 2023, **8**, 24256–24267.
22 O. ur Rahman, S. C. Mohapatra and S. Ahmad, *Mater. Chem. Phys.*, 2012, **132**, 196–202.
23 T. N. Ly and S. Park, *Sci. Rep.*, 2018, **8**, 18030.
24 T. N. Ly and S. Park, *J. Ind. Eng. Chem.*, 2018, **67**, 417–428.
25 R. Shokoohi, K. Godini and Z. Latifi, *Inorg. Chem. Commun.*, 2023, **149**, 110400.
26 V. S. Kore, S. D. Manjare and S. V. Taralkar, *J. Water Proc. Eng.*, 2023, **56**, 104472.
27 S. Ruiz, J. A. Tamayo, J. Delgado Ospina, D. P. Navia Porras, M. E. Valencia Zapata, J. H. Mina Hernandez, C. H. Valencia, F. Zuluaga and C. D. Grande Tovar, *Biomolecules*, 2019, **9**, 109.
28 N. M. S. Hidayah, W.-W. Liu, C.-W. Lai, N. Z. Noriman, C.-S. Khe, U. Hashim and H. C. Lee, *AIP Conf. Proc.*, 2017, **1892**, 150002.
29 A. A. Adu, Y. A. B. Neolaka, A. A. P. Riwu, M. Iqbal, H. Darmokoesoemo and H. S. Kusuma, *J. Mater. Res. Technol.*, 2020, **9**, 11060–11068.

30 W. C. Khoo, S. Kamaruzaman, H. N. Lim, S. N. A. Md. Jamil and N. Yahaya, *J. Polym. Res.*, 2019, **26**, 184.
31 K. Yang, H. Peng, Y. Wen and N. Li, *Appl. Surf. Sci.*, 2010, **256**, 3093–3097.
32 P. Kumar, M. Gupta, H. F. Hawari, V. Kumar and Y. K. Mishra, *Nano Express*, 2025, **6**, 025004.
33 P. Kumar, H. F. Hawari, M. Gupta, W. X. R. Leong, M. S. M. Saheed, G. M. Stojanović and L. I. Izhar, *J. Mater. Sci.*, 2024, **59**, 22132–22148.
34 G. Bhattacharya, S. Sas, S. Wadhwa, A. Mathur, J. McLaughlin and S. Sinha Roy, *RSC Adv.*, 2017, **7**, 26680–26688, DOI: **10.1039/C7RA02828H**.
35 A. Ganguly, S. Sharma, P. Papakonstantinou and J. Hamilton, *J. Phys. Chem. C*, 2011, **115**, 17009–17019.
36 H. Badenhorst, *Carbon*, 2014, **66**, 674–690.
37 K. Krishnamoorthy, M. Veerapandian, K. Yun and S.-J. Kim, *Carbon*, 2013, **53**, 38–49.
38 M. Farbod and M. Madadi Jaberi, *Fullerenes, Nanotubes Carbon Nanostruct.*, 2021, **29**, 244–250.
39 L. Zhang, G. Song, Z. Zhao, L. Ma, H. Xu, G. Wu, Y. Song, Y. Liu, L. Qiu and X. Li, *Gels*, 2022, **8**, 618.
40 C. Hu, Z. Gao and X. Yang, *Chem. Phys. Lett.*, 2006, **429**, 513–517.
41 A. Y. Lee, K. Yang, N. D. Anh, C. Park, S. M. Lee, T. G. Lee and M. S. Jeong, *Appl. Surf. Sci.*, 2021, **536**, 147990.
42 D. López-Díaz, M. López Holgado, J. L. García-Fierro and M. M. Velázquez, *J. Phys. Chem. C*, 2017, **121**, 20489–20497.
43 M. Gupta, H. F. Hawari, P. Kumar and Z. A. Burhanudin, *Crystals*, 2022, **12**, 264.
44 D. López-Díaz, M. López Holgado, J. L. García-Fierro and M. M. Velázquez, *J. Phys. Chem. C*, 2017, **121**, 20489–20497.
45 L. Wen, K. Li, J. Liu, Y. Huang, F. Bu, B. Zhao and Y. Xu, *RSC Adv.*, 2017, **7**, 7688–7693.
46 K. Ranganathan, A. Morais, I. Nongwe, C. Longo, A. F. Nogueira and N. J. Coville, *J. Mol. Catal. A: Chem.*, 2016, **422**, 165–174.
47 M. Gupta, H. F. Hawari, P. Kumar, Z. A. Burhanudin and N. Tansu, *Nanomaterials*, 2021, **11**, 623.
48 V. Urbanová, Š. Kment and R. Zbořil, *J. Electrochem. Soc.*, 2020, **167**, 116521.
49 P. Lv, X. Tang, R. Zheng, X. Ma, K. Yu and W. Wei, *Nanoscale Res. Lett.*, 2017, **12**, 630.
50 D. Wilson and M. A. Langell, *Appl. Surf. Sci.*, 2014, **303**, 6–13.
51 J. Yang, P. Zou, L. Yang, J. Cao, Y. Sun, D. Han, S. Yang, Z. Wang, G. Chen, B. Wang and X. Kong, *Appl. Surf. Sci.*, 2014, **303**, 425–432.
52 X. Shen, X. Lin, N. Yousefi, J. Jia and J.-K. Kim, *Carbon*, 2014, **66**, 84–92.
53 D. D'Angelo, C. Bongiorno, M. Amato, I. Deretzis, A. La Magna, G. Compagnini, S. F. Spanò and S. Scalese, *Carbon*, 2015, **93**, 1034–1041.
54 M. A. Worsley, P. J. Pauzauskie, T. Y. Olson, J. Biener, J. H. Satcher Jr and T. F. Baumann, *J. Am. Chem. Soc.*, 2010, **132**, 14067–14069.
55 Z.-Y. Sui, Q.-H. Meng, J.-T. Li, J.-H. Zhu, Y. Cui and B.-H. Han, *J. Mater. Chem. A*, 2014, **2**, 9891–9898.
56 S. Zhou, W. Jiang, T. Wang and Y. Lu, *Ind. Eng. Chem. Res.*, 2015, **54**, 5460–5467.
57 A. S. Carvalho, D. M. Oliveira, L. K. C. S. Assis, A. R. Rodrigues, P. L. Guzzo, L. C. Almeida and E. Padrón-Hernández, *J. Alloys Compd.*, 2023, **968**, 172038.
58 M. N. Nadagouda and R. S. Varma, *Cryst. Growth Des.*, 2007, **7**, 2582–2587.
59 M. J. Fernández-Merino, L. Guardia, J. I. Paredes, S. Villar-Rodil, P. Solís-Fernández, A. Martínez-Alonso and J. M. D. Tascón, *J. Phys. Chem. C*, 2010, **114**, 6426–6432.
60 M. F. Abdullah, R. Zakaria and S. H. S. Zein, *RSC Adv.*, 2014, **4**, 34510–34518.
61 Y. Guo, Q. Sun, F.-G. Wu, Y. Dai and X. Chen, *Adv. Mater.*, 2021, **33**, 2007356.
62 Y. Nosaka and A. Nosaka, *ACS Energy Lett.*, 2016, **1**, 356–359.
63 S. Gligorovski, R. Strekowski, S. Barbati and D. Vione, *Chem. Rev.*, 2015, **115**, 13051–13092.
64 Y. Qiu, Q. Zhang, Z. Wang, B. Gao, Z. Fan, M. Li, H. Hao, X. Wei and M. Zhong, *Sci. Total Environ.*, 2021, **758**, 143584.
65 C.-X. Chen, S.-S. Yang, J.-W. Pang, L. He, Y.-N. Zang, L. Ding, N.-Q. Ren and J. Ding, *Environ. Sci. Ecotechnology*, 2024, **22**, 100449.
66 R. Kumar, M. A. Barakat, B. A. Al-Mur, F. A. Alseroury and J. O. Eniola, *J. Cleaner Prod.*, 2020, **246**, 119076.
67 S.-P. Sun, C.-J. Li, J.-H. Sun, S.-H. Shi, M.-H. Fan and Q. Zhou, *J. Hazard. Mater.*, 2009, **161**, 1052–1057.
68 H. Kusic, D. Juretic, N. Koprivanac, V. Marin and A. L. Božić, *J. Hazard. Mater.*, 2011, **185**, 1558–1568.
69 M. Hou, F. Li, X. Liu, X. Wang and H. Wan, *J. Hazard. Mater.*, 2007, **145**, 305–314.